Accepted Manuscript

Investigating microstructural evolution during the electroreduction of UO_2 to U in LiCl-KCl eutectic using focused ion beam tomography

L.D. Brown, R. Abdulaziz, B. Tjaden, D. Inman, D.J.L. Brett, P.R. Shearing

PII: S0022-3115(16)30422-6

DOI: 10.1016/j.jnucmat.2016.07.036

Reference: NUMA 49843

To appear in: *Journal of Nuclear Materials*

Received Date: 4 February 2016

Revised Date: 12 July 2016

Accepted Date: 13 July 2016

Please cite this article as: L.D. Brown, R. Abdulaziz, B. Tjaden, D. Inman, D.J.L. Brett, P.R. Shearing, Investigating microstructural evolution during the electroreduction of UO_2 to U in LiCl-KCl eutectic using focused ion beam tomography, *Journal of Nuclear Materials* (2016), doi: 10.1016/j.jnucmat.2016.07.036.

Investigating Microstructural Evolution During the Electroreduction of UO_2 to U in LiCl-KCl Eutectic Using Focused Ion Beam Tomography

L.D.Brown[a], R.Abdulaziz[a], B.Tjaden[a], D.Inman[a], D.J.L.Brett[a], P.R.Shearing[a]

[a]Electrochemical Innovation Lab, Dept. Chemical Engineering, UCL, London, WC1E 7JE

Abstract

Reprocessing of spent nuclear fuels using molten salt media is an attractive alternative to liquid-liquid extraction techniques. Pyroelectrochemical processing utilizes direct, selective, electrochemical reduction of uranium dioxide, followed by selective electroplating of a uranium metal. Thermodynamic prediction of the electrochemical reduction of UO_2 to U in LiCl-KCl eutectic has shown to be a function of the oxide ion activity. The pO^{2-} of the salt may be affected by the microstructure of the UO_2 electrode. A uranium dioxide filled "micro-bucket" electrode has been partially electroreduced to uranium metal in molten lithium chloride-potassium chloride eutectic. This partial electroreduction resulted in two distinct microstructures: a dense UO_2 and a porous U metal structure were characterised by energy dispersive X-ray spectroscopy. Focused ion beam tomography was performed on four regions of this electrode which revealed an overall porosity ranging from 17.36% at the outer edge to 3.91% towards the centre, commensurate with the expected extent of reaction in each location. The pore connectivity was also seen to reduce from 88.32% to 17.86% in the same regions and the tortuosity through the sample was modelled along the axis of propagation of the electroreduction, which was seen to increase from a value of 4.42 to a value of infinity (disconnected pores). These microstructural characteristics could impede the transport of O^{2-} ions resulting in a change in the local pO^{2-} which could result in the inability to perform the electroreduction.

1. Introduction

Research into the reprocessing of spent nuclear fuel using molten salt media has become increasingly popular as an alternative to the PUREX process [1-3]. Spent oxide fuel must first be reduced to the metallic form prior to electrorefining. One technique of achieving this is via the addition of cadmium chloride to a LiCl-KCl eutectic (LKE) salt which serves to oxidise metallic spent fuel, resulting in U^{3+} and Pu^{3+} species in solution. These species are then recovered electrochemically at solid and liquid electrodes to acquire uranium and plutonium metals respectively [2, 4, 5]. The reduction of spent fuel oxides may also be done chemically via the reaction of dissolved lithium in LiCl at 650°C, as described by Karell and Gourishankar [6, 7]. Alternatively, spent fuel oxides may be reduced by electroplating Li metal onto the working electrode in a Li_2O containing LiCl molten salt, currently the more favoured route [8-11]. A further, fully electrochemical, technique is also under investigation: *pyroelectrochemical* processing. This technique aims to utilize selective electroreduction of spent fuel oxides followed by the successive, selective, electroplating of the metal in LKE [12, 13].The authors have shown that the direct electrochemical reduction of uranium dioxide to uranium metal in LKE at 450°C is feasible and appears to proceed via a single, 4-electron step process, with no observable intermediate compounds formed during the reduction [11]. This agrees with thermodynamic predictions [14, 15]. The use of LKE salt is advantageous compared to the LiCl melt due to its relatively low operating temperature and, therefore, operating costs. However, full scale operation using LKE may be limited in its application because of the limited solubility of Li_2O in LKE [16].

Littlewood diagrams [17] have also shown that the reduction process may be inhibited by the activity of O^{2-} ions in the bulk electrolyte. Too high a concentration of oxide ions may cause the $UO_2|U$ electrochemical reduction potential to become more cathodic than the deposition potential of lithium from the electrolyte. The microstructure of the electrode will affect the efficiency of the electrochemical reduction as characteristics of the microstructure (porosity, tortuosity, *etc.*) may impede the transport of electrolyte and/or O^{2-} ions out of the electrode, resulting in reduced three phase interlines (3PIs) and/or a local increase in the level of pO^{2-} within the electrode [18-20].

Considering that the microstructure of these electrodes is inherently a three-dimensional property, these electrodes must be studied in three dimensions in order to capture the true characteristics of the microstructure and to afford the ability to optimise the microstructure for the electroreduction process. In spite of its importance, there has been little research into the complex microstructure of these electrode materials, and to the authors' knowledge, the microstructure of electrodes for molten salt electroreduction have not yet been studied in three dimensions using tomography techniques. These tools have, however, been widely applied to other electrochemical devices, such as fuel cells and batteries [21-27]. Significant evolution of the microstructure is expected during the electroreduction of UO_2 to U due to the volume change associated with the reduction process: the molar volume of UO_2 is *ca.* 26.7 $cm^3\ mol^{-1}$ whereas the molar volume of U metal is *ca.* 12.5 $cm^3\ mol^{-1}$.

For the first time, three dimensional, focused ion beam (FIB) tomography has been utilised to understand the microstructural evolution during the electroreduction process: As UO_2 is reduced to U, a volume change is expected to occur, creating more pores. However, this microstrucrual reconstruction is currently poorly understood. Reconstruction of these volumes have been used to extract true microstructural characteristics and have also been modelled using the StarCCM software suite to extract the pore-phase tortuosity.

2. Experimental

2.1. Experimental set-up

The use of a molten LKE salt has an operational temperature sufficiently low to permit the use of glass in the experimental set-up. This has the advantage of optical accessibility to allow for rapid identification of the salt conditions, therefore, an all-glass electrochemical cell furnace were used for all electrochemical tests, which is described elsewhere [13]. A "micro bucket" electrode (MBE) was fabricated using a 3 mm diameter (10 mm long) molybdenum rod (>99%, Alfa Aesar). A 0.8 mm hole was drilled into the cross section of the rod, approximately 2 mm deep, into which UO_2 powder was pressed. This electrode is then attached to a similar molybdenum rod of greater length using a 0.2 mm molybdenum wire. This configuration is made the working electrode and can be seen in Figure 1. An all-glass $Ag|Ag^+$ reference electrode was also built, similar to that described in [28], which contained 0.75 mol kg^{-1} AgCl in LKE. A 3 mm diameter dense graphite rod (Alfa Aesar) was used as the counter electrode.

LiCl and KCl salts (>99%, Sigma-Aldrich) were dried under vacuum for 48 hours and transferred, under argon, to an argon-filled glove box with an atmosphere containing <0.5 ppm of both O_2 and H_2O, for storage. LKE (100 g) was mixed using a weighted molar average of 59% LiCl and 41% KCl and was placed into the reaction cell, inside the glove box. The cell was then sealed with a machinable ceramic (Pyrophyllite, Ceramic Substrates and Components Ltd.) cell head and PTFE gasket. The head contained holes for electrodes and gas lines with check valves to ensure a gas tight environment (see Fig. 1b).

Once the cell was sealed inside the glove box, it was transferred to a separate glove box which housed the optical furnace and a flow of argon gas (after purging the gas lines) was administered to the cell. Once the cell had reached the operating temperature of 450°C, the UO_2 –filled MBE was rapidly inserted into the cell and left to thermally stabilise for 30 minutes. Finally, the working electrode was immersed into the molten salt and left to thermally stabilise. Electrochemical measurements were taken using an IVIUMStat potentiostat (IVIUM Technologies).

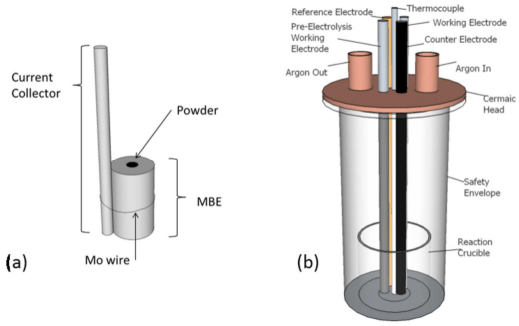

Fig. 1. Illustration of the micro-bucket electrode configuration, powder is pressed into a 0.8 mm OD (2 mm) L hole drilled into a molybdenum rod.

2.2. FIB Tomography

FIB Tomography was performed using the "slice and view" technique [29]. During this process, the face of interest is first imaged with an SEM before it is milled by a predetermined depth using a gallium ion beam. The new exposed face of interest is then image and this process is repeated, giving rise to a stack of images. These images may then be stacked together to produce a three-dimensional representation of the sample volume. During FIB tomography, a trench should be milled in order to expose a region of interest [30]. In the case of this study, a 50 × 150 × 20 µm (xyz) trench was milled using the FIB (Carl Zeiss XB1540 Cross-Beam focussed-ion-beam microscope (Carl Zeiss AG)) with a beam current of 5 nA.

SEM imaging was acquired using the SE2 detector, an acceleration voltage of 5 keV and a working distance of 5 mm, resulting in a pixel size of 90 nm. The sample was aligned to permit FIB tomography reconstructions from the edge of the sample to the centre using the "slice and view" technique, with each "slice" being 90 nm in depth.

The image stacks were imported into the Avizo Fire 8 (FEI) software suite for segmentation of the pore phase and for three-dimensional reconstruction. A label analysis was then conducted on each sample which deduces which pores are connected (based on a 24 voxel neighbourhood) and results in each connected pore being assigned a new colour, allowing for visual identification of the pore connectivity.

3. Results and discussion

3.1. Cyclic voltammetry on UO_2 electrodes

Cyclic voltammetry was performed on the UO_2 working electrode, which is presented in Figure 2. Peaks C1 and A1 are attributed to reduction and oxidation processes occurring on the molybdenum current collector, respectively. The reduction peak C2 is attributed to the electrochemical reduction of UO_2:

$$UO_2 + 4e^- \rightarrow U + 2O^{2-} \qquad \text{Eq. (1)}$$

This reduction peak is in close proximity to the deposition potential of lithium, C3. From this, the pO^{2-} of the melt has been calculated from Littlewood diagrams to be equal to 6 [15]. In addition, there is no observable oxidation peak on the anodic scan of the UO_2 filled working electrode. This suggests that the oxygen anions that have been liberated due to the reduction have diffused away from the boundary of the powder. Therefore, these oxygen anions are not available at the working electrode to re-oxidise the uranium and would explain the omission of an oxidation peak associated with uranium. It is also possible that any Li deposition in contact with the UO_2 from peak C3 (reduction of Li^+ from the electrolyte) would react chemically with uranium dioxide via the Eq. 2

$$UO_2 + 4Li \rightarrow U + 2Li_2O \qquad \text{Eq (2)}$$

Li_2O is soluble in LKE (albeit lowly) and is a possible side reaction which would also cause omission of an oxidation peaks in the CV [16].

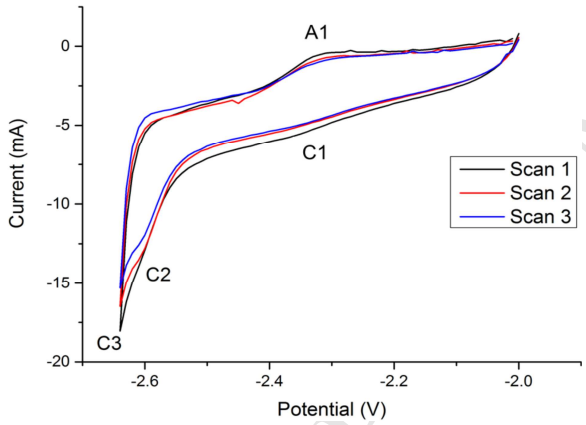

Fig. 2. A three scan cyclic voltammogram of the UO_2-filled MBE working electrode (graphite counter electrode) at 10 mV s^{-1}. Potentials are reported with respect to the $Ag|Ag^+$ reference electrode. C2 is attributed to the electrochemical reduction of UO_2 to U

The resulting, partially reduced, electrode was removed from the molten salt cell and placed in methanol for a week to dissolve the solidified melt. The electrode was then impregnated in epoxy and polished before being analysed using scanning electron microscopy, as shown in Figure 3(a). From this, it is possible to identify two regions: a dense region towards the centre of the electrode and a more porous region towards the edge. This is similar to the dense and "coral-like" structures observed by Kurata *et al.* [11].

Energy dispersive X-ray spectroscopy (EDS) was performed on both the dense phase and on the "coral-like" phase and is shown in Figure 3(b). Observation of these spectra shows that the porous phase has no identifiable oxygen peak, indicating the material nearest the edge has undergone complete reduction to metallic uranium whilst the material towards the centre of the electrode has

not been reduced and the oxide remains. This is in agreement with the three phase interline theory described by Qiu *et al.,* [31].

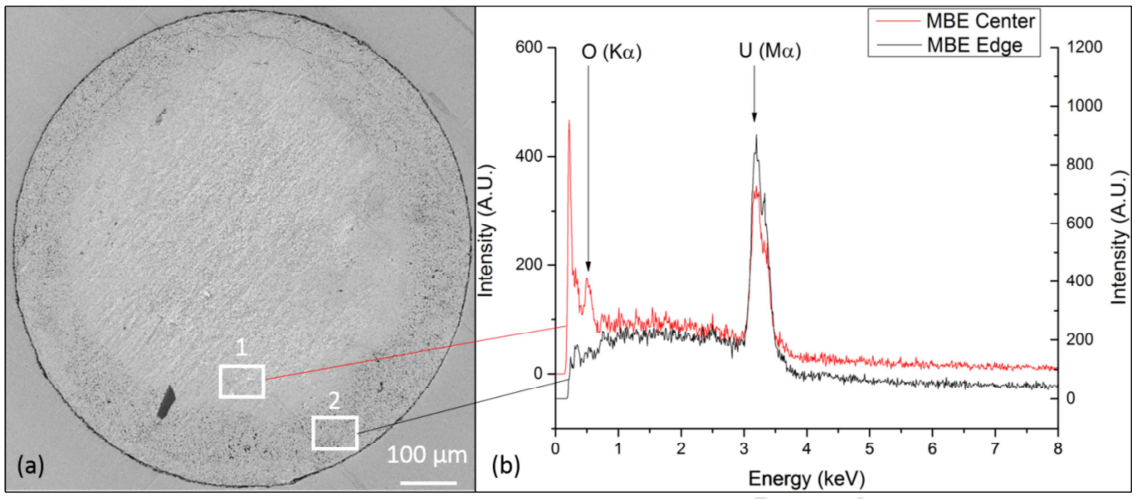

Fig. 3. (a) "Birds-eye view" of the MBE working electrode after cyclic voltammetry. There is a porous phase towards the outer edge and a denser phase towards the centre. EDS was performed on the regions depicted by boxes 1 and 2 and is shown in (b). The EDS spectra show no observable O (Kα) peak on the outer edge region, indicating that this region has been reduced.

3.2. Porosity and pore connectivity

A total of five reconstructed regions of the partially reduced sample were reconstructed each with a voxel size of 90 × 90 × 90 nm^3. The first four regions were a porous, structure, whilst the last reconstruction was of the dense phases. The porous structures may be seen to be similar to the coral-like structures observed by Kurata *et al.* [11]. An SEM micrograph depicting the five reconstructed regions is shown in Figure 4.

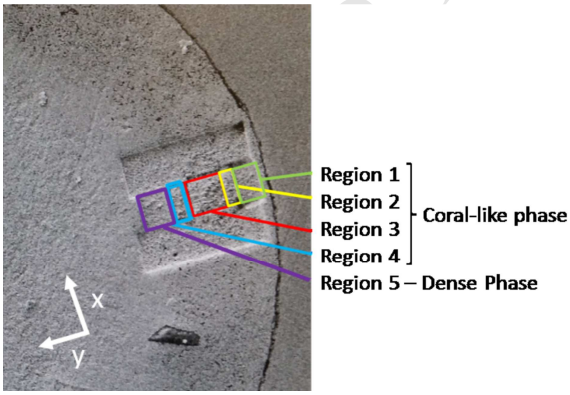

Fig. 4. Milled trench generated using the FIB. Five regions were reconstructed from this and these are labelled as regions 1-5.

The result of the slice and view technique is a stack of images of the sample along the y-axis. A sample "slice" has been reproduced in Figure 5(a). The regions of interest in the images were then cropped (*e.g.* Figure 5(b)) and aligned before a histogram equalisation filter was applied resulting in Figure 5(c). This filter improves the contrast in the images: the pixel count histogram for the unfiltered image is shown in Figure 5(e), whilst that of the filtered image is shown in Figure 5(f). Lastly, the images were converted into binary images by threshold segmentation, as shown in Figure 5(d).

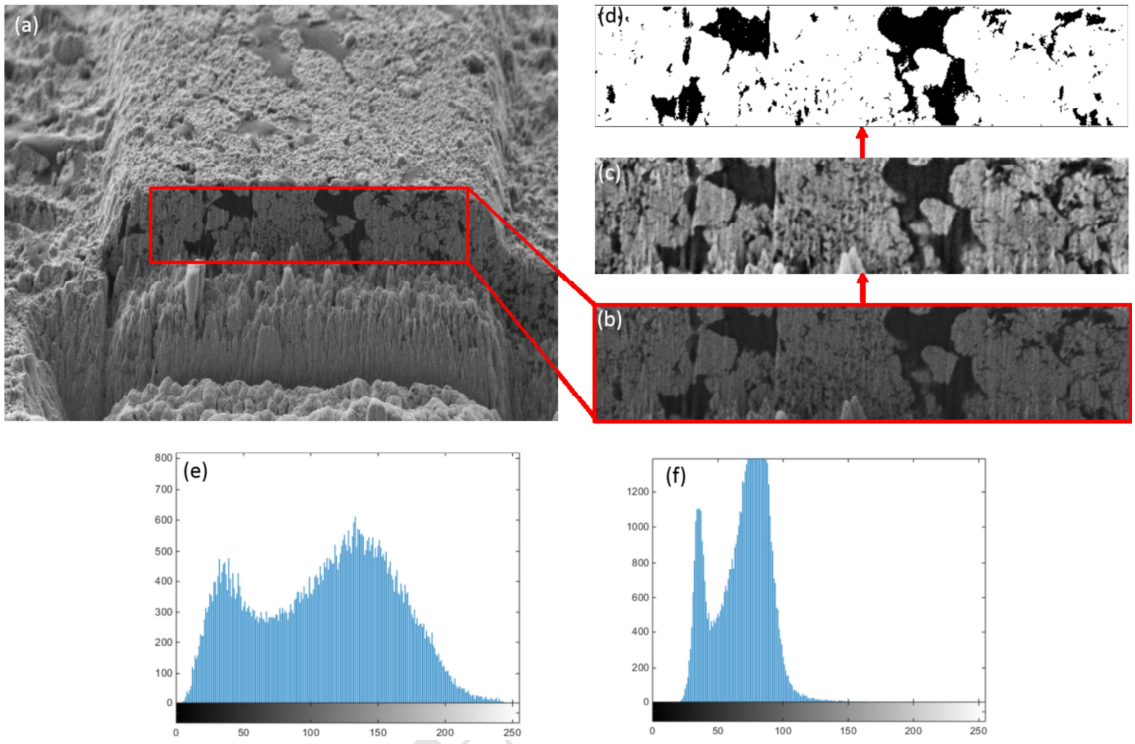

Fig. 5. (a) Raw image of the sample during FIB tomography. The region of interest is cropped (b) and was then subjected to an adaptive histogram equalization filter, resulting in (c). (d) Shows the final binarised image used for three-dimensional reconstruction. (e) Pixel count histogram of the original cropped image and (f) shows the pixel count histogram after the filter was applied, allowing for good segmentation of the phases.

A reconstruction of Region 1 is presented in Figure 6 and shows the segmented porous phase of the sample where each connected pore has been assigned a different colour. The high pore connectivity of this region is indicated by the large turquoise coloured pore. Also presented in Figure 6(c) and (d) are skeletonization projections of the pore phase: these projections visualise the centreline of interconnected pores as thinned filaments. That is, the centreline of the porous phase is displayed as a network of filaments which help to represent the centroid pathways of the pore network. A high density of these filaments is representative of high spatial porosity and a well-connected pore system; whereas a low density is indicative of a low spatial porosity. The absence of these filaments represents the solid phase of the material.

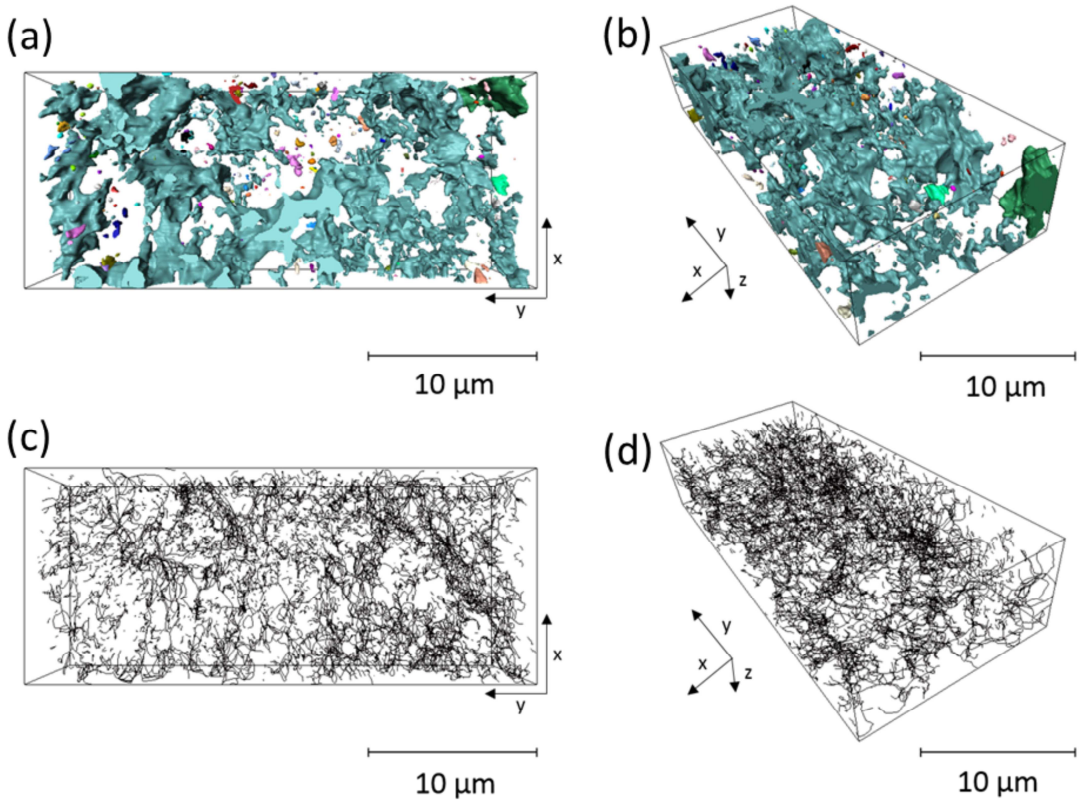

Fig. 6. Region 1 of the partially reduced MBE showing the pore phase in: (a) the XZ plane and (b) the XYZ plane. (c) Shows a skeletization of the pore phase in the XZ plane and (d) in the XYZ plane.

The pore connectivity of region one was extracted to be equal to 88.3%. This is calculated by taking the largest volume pore and dividing by the total volume of the pores. High pore connectivity would permit good diffusion of species through the microstructure. The overall porosity was also extracted to be equal to 17.4%, a ratio of the volume occupied by pores to the total volume of the sample.

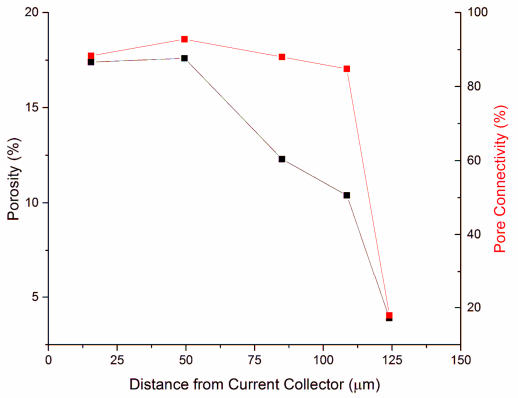

Fig. 7. Volume fraction porosity and the pore connectivity as a function of distance from the current collector in the y-direction. A significant change in porosity and pore connectivity is observed.

This method was repeated for all sample regions and the overall porosity and pore connectivity values, as a function of distance from the current collector, are shown in Figure 7. Up to a distance of *ca.* 50 µm from the current collector (Regions 1 and 2), similar microstructural characteristics may be observed; however, as the distance increases to > 50 µm (Regions 3 onwards) a decrease in both the porosity and the pore connectivity is apparent. At a distance of *ca.* 125 µm, (Region 5), which is unreduced UO_2, shows an even more significant decrease in porosity and pore connectivity. This is consistent with a large extent of reduction at the electrode edge, which is diminished towards the centre region of the electrode: a general trend of decreasing porosity and pore connectivity may be observed from the outer edge towards the centre of the MBE. This trend is indicative of the electrochemical reduction propagating through the MBE electrode, from the edge to the centre, following the three phase interline theory, which is described in more detail below. The porosity change is attributed to the volume change associated with the reduction of uranium dioxide: as the electroreduction from UO_2 to U occurs, porosity within the microstructure is produced, facilitating the transport of O^{2-} ions through the microstructure. However, the decreased pore connectivity towards the centre of the MBE may have consequences on the efficiency of the electroreduction process. It is apparent that the microstructure of the electrode is a function of the electroreduction front moving inwards. A decrease in pore connectivity, due to the reduction front, may impede the transport of O^{2-} ions out of the electrode and may lead to an increase in the level of pO^{2-}, which could impede of the electroreduction process.

3.3. Tortuosity simulations

The tortuosity, τ, plays an essential role in characterising the transport of species through the microstructure and quantifies the resistance of such a structure to mass transport. This encompasses, among others, the migration of electrons, ions, gases and heat. The tortuosity is geometrically defined as the shortest path length through a porous structure divided by the normal, straight line, distance between the end points of that path resulting in τ being always greater than or equal to one [32]. In terms of transport, this would be proportional to the effective cross sectional area and inversely proportional to the length of the pore. In addition, for a given pore of fixed volume, doubling the length of the pore will result in a halving of the cross section. Therefore, the

effect of a change in transport will be squared due to the change in extra path length between two points [33-35]. These two definitions are of the tortuosity and the tortuosity factor, respectively.

The measurement of tortuosity is not trivial: several different methods have been developed, among which image based modelling of transport phenomena, is one [36, 37]: achieved by using the analogy of Ficks' and Fourier's laws in the StarCCM+ computational fluid dynamics (CFD) package.

For this, a surface mesh was created from the tomography data set in Avizo Fire 8 and imported via a .STL file type, into the StarCCM+ CFD software package. A volume mesh was then created to enable transport modelling through the pore phase. The tortuosities in each direction (τ_x, τ_y and τ_z) may be calculated by modelling the heat flux through the surfaces in the required axis and keeping all other surfaces adiabatic. The tortuosities may then be extracted by the application of the following equation:

$$\tau = \sqrt{\epsilon \frac{Q_{CV}}{Q_{Pore}}} \quad \text{Eq. 3}$$

Where τ is the tortuosity, ε is the porosity, Q_{CV} is the flux through the control volume and Q_{Pore} is the flux through the pore phase. For derivation of this equation, the reader is referred to [37]. Figure 8(a) shows an example surface mesh reconstruction, while Figure 8(b) shows the 'temperature' distribution across the sample reconstruction after converged heat flux simulation. This methodology was applied to all axes for each reconstruction. These results are tabulated in Table 1; note, that only the connected pore phase was extracted as the inclusion of other pores would cause non-divergence in the CFD calculations and would not influence transport.

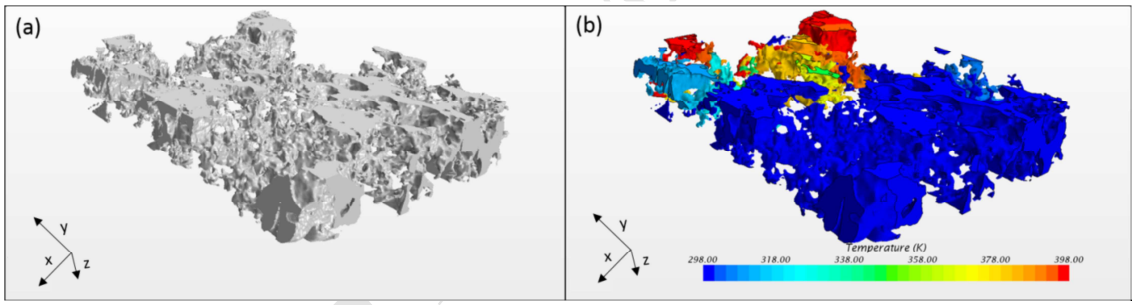

Figure 8 (a) An example surface mesh reconstruction and (b) an example of heat flux simulation through the y axis.

The tortuosities calculated have been tabulated in Table 1 which shows that after Region 1 more significant tortuosity values are present in each direction. These relatively large tortuosities would provide resistance to molten salt penetration and significant inhibition of the transport of O^{2-} ions away from the active reaction sites. In turn, this could lead to a reduction in the local level of the pO^{2-}, resulting in a change in the potential for electrochemical reduction. An infinite tortuosity represents no pore connectivity in that direction. In such a case, molten salt penetration would not occur through that direction, meaning no electroreduction could occur.

Region	τ_x	τ_y	τ_z
1	1.46	4.42	12.41
2	18.85	3.68	12.93
3	15.02	7.22	∞

4	∞	∞	∞
5	∞	∞	∞

Table 1. Tortuosity values calculated along each axis for the four reconstructed regions. Note that a value of infinity represents the CFD calculations being unable to diverge.

A three phase interline (3PI) is defined as a region whereby all three of the necessary phases co-exist which is a pre-requisite for the electrochemical reduction to occur [18-20]. In the context of metal oxide electroreduction in a molten salt, the 3PI is formed of an electronic conducting phase, which provides electrons to perform the reduction; an ionic conducting phase, which allows oxide ions to be removed via the melt, and the metal oxide phase, which is to be electroreduced. Only at these 3PIs will an electrochemical reduction be able to occur.

The 3PI theory predicts that the electrochemical reduction would propagate radially from the current collector edge, to the centre of the MBE. This would be along the y-direction defined in Figure 4. By observation of the tortuosity in this direction, τ_Y, for all reconstructed volumes it is seen to decrease from a value of 4.42 in Region 1 to a value of 3.68 in Region 2. This follows the trend of increased porosity and pore connectivity between the two regions. However, the value increases significantly from 3.68 in Region 2 to a value of 7.22 in Region 3. This, again, follows the decrease in porosity and pore connectivity, which reveals a much more tortuous route for the transport of O^{2-} ions. These high tortuosity values are explained in Figure 7: although the pore connectivity of the entire sample was extracted to be 92.78%, the connectivity between pores is maintained by a single pore channel, as depicted in Figure 9. Consequently, although the total pore connectivity is high, the transport of O^{2-} ions through this pore phase in the y-direction would be impeded. Region 4 of the reconstruction possesses infinite tortuosity values for each direction due to the lack of pore connectivity of the sample. This is again seen in Region 5 (the unreduced region). If the reduction front doesn't improve the pore connectivity in this region, the transport of O^{2-} ions out of the electrode will be impeded. In order for the electrochemical reduction of UO_2 to U metal to proceed to completion, pores must be connected during the volume change associated with the electroreduction. However, a possible solution to this would be to produce connected pore phase microstructure within the UO_2 phase. This will ensure that transport of O^{2-} ions from the electrode to the counter electrode is not governed by pores becoming connected due to the volume change during electroreduction.

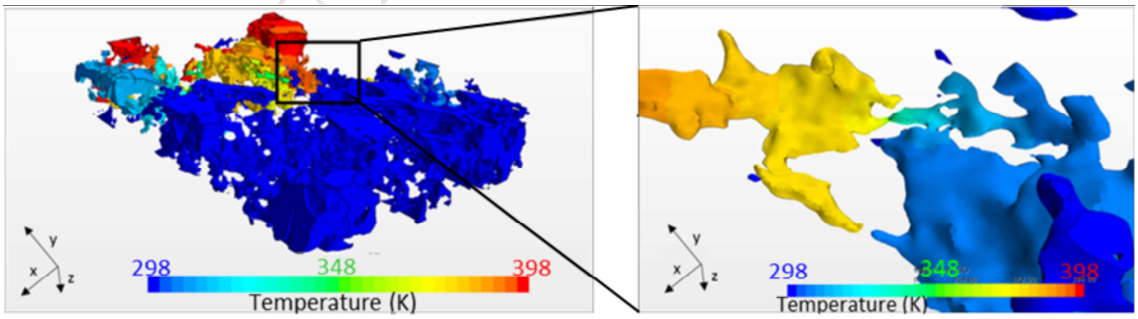

Fig. 9. Heat flux through the y-axis direction in Region 2. The blown up region shows only a single channel of pore connectivity through the sample.

4. Conclusion

For the first time, the microstructure of partially reduced uranium oxide electrodes has been studied. The porosity along the axis of the propagation of the electrochemical reduction was seen to reduce significantly with the extent of the electroreduction. Additionally, the tortuosity in this plane was also seen to increase from a value of 4.42 to an infinite tortuosity in the dense phase of un-reduced sample. This microstructural phenomenon may impede the transport of O^{2-} ions from the bulk electrode which would decrease the local value of pO^{2-}. This is a dynamic variable which would change as the electroreduction propagates throughout the bulk electrode. Because of this, it is suggested that the diffusion of O^{2-} ions away from the electrode would be dependent on the volume change during electroreduction, causing the isolated pores to become connected. This highlights the need to understand and optimise electrode microstructure to enhance 3PIs and the electroreduction process.

Acknowledgements

This work was carried out as part of the UK Engineering and Physical Sciences Research Council (EPSRC) funded REFINE consortium (http://www.refine.eng.ed.ac.uk/). We gratefully acknowledge the EPSRC for financial support of the spent nuclear waste processing research in the Electrochemical Innovation Lab (EP/J000531/1; EP/L018616/1). PRS thanks the Royal Academy of Engineering for financial support. We dedicate this publication to the memory of Professor Douglas Inman.

References

[1] Koyama T, Iizuka M, Shoji Y, Fujita R, Tanaka H, Kobayashi T, Tokiwai M. Journal of Nuclear Science and Technology 1997;34:384.
[2] Pierce RD, Johnson TR, Mcpheeters CC, Laidler JJ. Jom-J Min Met Mat S 1993;45:40.
[3] Iizuka M, Inoue T, Ougier M, Glatz J-P. Journal of Nuclear Science and Technology 2007;44:801.
[4] Laidler JJ. Development of IFR pyroprocessing technology

Proceedings of Global 1993 Conference - Future Nuclear Systems: Emerging Fuel Cycles and Disposal Options, 1993.
[5] Laidler J, Battles J, Miller W, Ackerman J, Carls E. Progress in Nuclear Energy 1997;31:131.
[6] Karell E, Gourishankar K, Johnson G. Electrometallurgical treatment of TMI-2 fuel debris. Argonne National Lab., IL (United States), 1997.
[7] Karen E, Gourishankar K, Chow L, Everhart R. GLOBAL '99 Conference 1999.
[8] Hur J-M, Seo C-S, Hong S-S, Kang D-S, Park S-W. Reaction Kinetics and Catalysis Letters 2003;80:217.
[9] Seo CS, Park SB, Park BH, Jung KJ, Park SW, Kim SH. Journal of Nuclear Science and Technology 2006;43:587.
[10] Jeong SM, Shin H-S, Hong S-S, Hur J-M, Do JB, Lee HS. Electrochimica Acta 2010;55:1749.
[11] Kurata M, Inoue T, Serp J, Ougier M, Glatz J-P. J Nucl Mater 2004;328:97.
[12] Hu D, Stevenson A, Chen GZ. ECS Transactions 2014;64:585.

[13] Brown LD, Abdulaziz R, Jervis R, Bharath VJ, Atwood RC, Reinhard C, Connor LD, Simons SJR, Inman D, Brett DJL, Shearing PR. J Nucl Mater 2015;464:256.
[14] Martinot L, Fuger J. Journal of the Less-Common Metals 1986;120:255.
[15] Brown LD, Abdulaziz R, Simons S, Inman D, Brett DJL, Shearing PR. J Appl Electrochem 2013;43:1235.
[16] Kado Y, Goto T, Hagiwara R. Journal of Chemical & Engineering Data 2008;53:2816.
[17] Littlewood R. Journal of The Electrochemical Society 1962;109:525.
[18] Deng Y. The journal of physical chemistry. B 2005;109:14043.
[19] Xiao W, Xiao X, Jin Y, Deng D, Wang G, Chen. Chemistry - A European Journal 2007;13:604.
[20] Xiao W, Xiao X, Jin Y, Deng D, Wang X, Hu G, Chen. ChemPhysChem 2006;7:1750.
[21] Shearing PR, Bradley RS, Gelb J, Lee SN, Atkinson A, Withers PJ, Brandon NP. Electrochem Solid St 2011;14:B117.
[22] Shearing PR, Bradley RS, Gelb J, Tariq F, Withers PJ, Brandon NP. Solid State Ionics 2012;216:69.
[23] Shearing PR, Golbert J, Chater RJ, Brandon NP. Chemical Engineering Science 2009;64:3928.
[24] Clague R, Shearing PR, Lee PD, Zhang Z, Brett DJL, Marquis AJ, Brandon NP. Journal of Power Sources 2011;196:9018.
[25] Eastwood DS, Bayley PM, Chang HJ, Taiwo OO, Vila-Comamala J, Brett DJ, Rau C, Withers PJ, Shearing PR, Grey CP. Chemical Communications 2015;51:266.
[26] Eastwood DS, Bradley RS, Tariq F, Cooper SJ, Taiwo OO, Gelb J, Merkle A, Brett DJL, Brandon NP, Withers PJ, Lee PD, Shearing PR. Nuclear Instruments and Methods in Physics Research Section B: Beam Interactions with Materials and Atoms 2014;324:118.
[27] Trogadas P, Taiwo OO, Tjaden B, Neville TP, Yun S, Parrondo J, Ramani V, Coppens M-O, Brett DJL, Shearing PR. Electrochemistry Communications 2014;48:155.
[28] Bockris JOM, Bockris GJ, Hills D, Inman L, Young. Journal of Scientific Instruments (1950) 1956;33:438.
[29] Uchic MD, Holzer L, Inkson BJ, Principe EL, Munroe P. MRS Bulletin 2007;32:408.
[30] Holzer L, Cantoni M. Nanofabrication Using Focused Ion and Electron Beams: Principles and Applications 2011;559201222.
[31] Qiu G, Qiu M, Ma D, Wang X, Jin X, Hu G, Chen. Journal of The Electrochemical Society 2005;152:E328.
[32] Cecen A, Wargo E, Hanna A, Turner D, Kalidindi S, Kumbur E. Journal of The Electrochemical Society 2012;159:B299.
[33] Epstein N. Chemical Engineering Science 1989;44:777.
[34] Tjaden B, Cooper SJ, Brett DJL, Kramer D, Shearing PR. Opinion in Chemical Engineering;Under Review.
[35] Tjaden B, Jonathan L, Withers PJ, Bradley RS, Brett DJL, Shearing PR. Solid State Ionics 2016;In Press.
[36] Wilson JR, Kobsiriphat W, Mendoza R, Chen H-Y, Hiller JM, Miller DJ, Thornton K, Voorhees PW, Adler SB, Barnett SA. Nature materials 2006;5:541.
[37] Cooper S, Eastwood D, Gelb J, Damblanc G, Brett D, Bradley R, Withers P, Lee P, Marquis A, Brandon N. Journal of Power Sources 2013;247:1033.

Highlights

- The microstructural evolution of the reduction from UO_2 to U has been investigated
- The porosity and tortuosity is seen to change significantly during electroreduction
- Low porosity and high tortuosity associated with the UO_2 phase may impede O^{2-} transport